

## Geophysical Research Letters®



#### RESEARCH LETTER

10.1029/2025GL116056

#### **Key Points:**

- Ascending motion associated with tropical rainfall extremes exhibit two distinct modes: stratiform decay and convective decay
- In Stratiform decay, environmental conditions disfavor convection, and the ascent profile becomes increasingly top-heavy
- Convective decay maintains bottomheavy ascent and prolonged rain, representing just over half of extreme events and extreme rainfall

#### Correspondence to:

Y.-X. Li, Yi-Xian.Li@monash.edu

#### Citation:

Li, Y.-X., Singh, M. S., Masunaga, H., & Yu, J.-Y. (2025). Bimodal evolution of vertical motion in tropical precipitation extremes. *Geophysical Research Letters*, 52, e2025GL116056. https://doi.org/10.1029/2025GL116056

Received 19 MAR 2025 Accepted 19 OCT 2025

# **Bimodal Evolution of Vertical Motion in Tropical Precipitation Extremes**

Yi-Xian Li<sup>1</sup>, Martin S. Singh<sup>1,2</sup>, Hirohiko Masunaga<sup>3</sup>, and Jia-Yuh Yu<sup>4</sup>

<sup>1</sup>School of Earth, Atmosphere and Environment, Monash University, Melbourne, VIC, Australia, <sup>2</sup>Australian Research Council Centre of Excellence for Weather in the 21st Century, Monash University, Melbourne, VIC, Australia, <sup>3</sup>Institute for Space-Earth Environmental Research, Nagoya University, Nagoya, Japan, <sup>4</sup>Department of Atmospheric Sciences, National Central University, Taoyuan, Taiwan

**Abstract** This study examines the evolution of "top-heaviness" in tropical convection during extreme precipitation events. Top-heaviness describes the extent to which ascent peaks in the upper (top-heavy) versus lower (bottom-heavy) troposphere. Reanalysis vertical velocity profiles are projected onto two sinusoidal basis functions, representing the first and second baroclinic modes, that together characterize top-heaviness. Two distinct modes are found following the peak in rainfall: stratiform decay and convective decay. Stratiform-decay events transition rapidly from bottom-heavy to top-heavy to stratiform-like ascent profiles and experience sharp reductions in instability, moisture and precipitation after the peak of the event. In contrast, convective-decay events sustain bottom-heavy ascent profiles with a gradual decline in instability and moisture and prolonged precipitation; they contribute over 55% of the rainfall during extreme events. These findings emphasize the significant role of convective decay in shaping extreme precipitation compared to conventional stratiform decay.

Plain Language Summary Heavy rain comes from rising air in the lowest layer of the atmosphere, called the troposphere. This is where clouds form and weather happens. Scientists have long focused on one common pattern: after rainfall reaches its peak, the strongest rising air shifts from the lower troposphere to the upper troposphere, eventually leaving behind clouds high in the sky. Here, we call this stratiform decay. Our study takes a closer look at how air motions evolve over time on a fine, hourly scale for tropical extreme rainfall events. We find another, more important pattern: convective decay. In this case, the strongest rising air stays in the lower troposphere in the hours following peak precipitation, without shifting upward, leading to extended periods of heavy rain. We show that convective decay produces more than half of the rainfall in extreme events, meaning it plays a larger role than stratiform decay.

#### 1. Introduction

Convection is a key process in the Earth's atmosphere, driving energy transport and playing a central role in the global water cycle. In the tropics, convective precipitation associated with deep and organized convective systems accounts for approximately half of the total rainfall (Lee et al., 2013; Rossow et al., 2013; Tan et al., 2015), while convection more broadly—including both convective and stratiform precipitation—contributes the vast majority of tropical rainfall. The vertical structure of convective systems—characterized by vertical velocity and thermodynamic variables such as moist static energy—determines how heat and moisture are redistributed from the lower to the upper troposphere, shaping energy transport and how convection interacts with the large-scale atmospheric circulation (Back & Bretherton, 2006; Chen & Yu, 2021; Inoue & Back, 2015a). A critical feature of convective systems is the extent to which large-scale vertical motion, which represents an average of updrafts in convective cores and surrounding subsidence, is concentrated in the upper troposphere compared to the lower troposphere, a characteristic termed "top-heaviness"; Top-heavy convection features the strongest upward motion in the upper troposphere, whereas bottom-heavy convection exhibits the strongest upward motion in the lower troposphere.

Most studies on top-heaviness have focused on its long-term climatology by quantifying empirical leading-mode amplitudes of vertical velocity across geographic locations (Back et al., 2017). For instance, within the ITCZ, the western Pacific is often characterized as more top-heavy than the eastern Pacific (Back & Bretherton, 2006; Back et al., 2017; Bernardez & Back, 2024). While theories attempting to explain these differences exist, (Back &

© 2025. The Author(s).
This is an open access article under the terms of the Creative Commons
Attribution License, which permits use, distribution and reproduction in any medium, provided the original work is properly cited.

LI ET AL.

Bretherton, 2009; Bernardez & Back, 2024; Neogi & Singh, 2022; Singh & Neogi, 2022), they remain semi-empirical or limited in scope.

The temporal evolution of top-heaviness is usually considered from the perspective of the vertical structure of diabatic heating within different types of clouds: convective and stratiform. Observations of diabatic heating profiles within convective regions reveal a characteristic temporal transition: from bottom-heavy heating to top-heavy heating, and eventually to upper-atmospheric heating with cooling below (Inoue et al., 2020; Lin et al., 2004; Mapes & Houze, 1995; Zhang & Hagos, 2009). Under weak temperature gradient assumptions—where heating is balanced by vertical advection of potential temperature—each heating profile generates a corresponding vertical velocity distribution reflective of the shape of heating scaled by the static stability (Sobel et al., 2001). As a result, the life cycle of tropical deep convection is generally thought to progress through these stages: bottom-heavy shallow convection, intermediate congestus convection, top-heavy deep convection, and stratiform clouds characterized by opposing vertical motions of upper-atmospheric ascent and lower-atmospheric descent. Despite differences in spatial and temporal scale, this evolutionary pattern is consistently observed across various convective phenomena, including convectively coupled equatorial waves, mesoscale convective systems (MCSs), and the Madden–Julian Oscillation (Benedict & Randall, 2007; Johnson et al., 1999; Kiladis et al., 2009; Mapes et al., 2006; Riley et al., 2011; Takayabu et al., 1996).

Previous studies often focus on specific phenomena such as tropical waves or large-scale convective systems, but few systematically analyze the broad range of extreme precipitation events. This study takes a comprehensive approach by examining all tropical rainfall extreme events, regardless of their inducing mechanisms. Leveraging high-temporal-resolution reanalysis data, we investigate whether the characteristic top-heaviness transition emerges as a robust feature across extreme events. This is motivated by the strong observed correlation between vertical updrafts and rainfall intensity (e.g., Gu et al., 2023; O'Gorman & Schneider, 2009a, 2009b) and by evidence that the most intense deep convection can rapidly modify surrounding free-tropospheric thermodynamic structures within hours of peak rainfall (Li et al., 2024). To visualize the temporal evolution of top-heaviness from multi-dimensional vertical velocity data, we introduce the top-heaviness plane, a novel diagnostic inspired by the gross moist stability plane (Inoue & Back, 2015b, 2017; Tsai & Yu, 2023). This tool simplifies complex vertical velocity patterns, revealing two distinct convective decay modes: stratiform decay, which follows the conventional bottom-heavy to top-heavy to stratiform-like transition, and convective decay, which maintains bottom-heavy ascent and contributes over half of the rainfall in extreme events.

The rest of this paper is organized as follows: Section 2 describes the data, Section 3 details the top-heaviness plane, Section 4 presents the findings, and Section 5 concludes with key insights.

#### 2. Data

This study primarily examines pressure-coordinate vertical velocity and precipitation from the European Centre for Medium-Range Weather Forecasts' fifth global reanalysis (ERA-5; Hersbach et al., 2020). Additionally, we use ERA-5's pressure-level fields of relative humidity, temperature, specific humidity, and geopotential fields to derive environmental variables of instability and plume buoyancy. The ERA5 data set is provided at hourly temporal frequency on a  $0.25^{\circ} \times 0.25^{\circ}$  grid. We focus on the period from 2001 to 2010 and the region 30°N to 30°S. To reduce the computational cost, we subsample the data by selecting every fourth grid point in both latitude and longitude. This approach yields information on a  $1^{\circ} \times 1^{\circ}$  grid.

#### 3. Top-Heaviness Plane and Top-Heaviness Angle

Top-heaviness refers to the strength of upward air motion in the upper troposphere compared to the lower troposphere. Convection is considered "top-heavy" when the vertical ascent is more intense in the upper troposphere, and "bottom-heavy" when the vertical ascent is more intense in the lower troposphere. To quantify top-heaviness, we follow two previous studies to introduce the top-heaviness angle and top-heaviness plane.

Following a similar approach to Masunaga & L'Ecuyer (2014), we project the vertical profile of pressure-coordinate vertical velocity  $\omega$  in the troposphere on two basis functions defined by a half and full sine wave, respectively:

LI ET AL. 2 of 13

$$\omega_2 = -\sin\left(2\pi \frac{p - p_t}{p_b - p_t}\right),\tag{2}$$

Here we set  $p_b = 1000$  hPa and  $p_t = 100$  hPa. The first basis function  $\omega_1$  corresponds to vertical motion with a single sign throughout the troposphere, peaking at 550 hPa. We refer to this as the first baroclinic mode. The second basis function  $\omega_2$  is characterized by opposing vertical velocities in the upper and lower troposphere. This is termed the second baroclinic mode.

By projecting a given pressure-coordinate vertical velocity profile between  $p_b$  and  $p_t$  onto these modes, we quantify how much of its structure aligns with each mode. The resulting amplitudes form a point on the top-heaviness plane, a two-dimensional phase space where the x-axis represents the first mode amplitude and the y-axis represents the second mode amplitude. The variance explained by each mode is given by the ratio of the squared sum of projected velocity values to that of the raw vertical velocity values across all levels. As we will show, decomposing the raw profiles into these two modes captures most of the variability, confirming that the top-heaviness plane effectively simplifies and visualizes the strength and vertical structure of vertical velocity.

In the top-heaviness plane, the top-heaviness angle is defined as the angle measured from the x-axis to the line connecting the origin to any projected point, with positive angles measured counterclockwise and negative angles measured clockwise (Figure 1a), as described by Bernardez and Back (2024). Spanning from  $-180^{\circ}$  to  $180^{\circ}$ , the top-heaviness angle provides a useful summary of the shape of the vertical velocity profile. For example, an angle of  $0^{\circ}$  is typically linked to deep convection with a middle-heavy vertical velocity profile, with upward motion throughout the troposphere and a peak in the middle troposphere. Although profiles with angles close to zero could reasonably be described as "middle-heavy," and such terminology has been used in previous studies, we classify these profiles simply as either top-heavy or bottom-heavy based on the top-heaviness angle. This binary classification allows us to emphasize the contrast between upper- and lower-tropospheric ascent, which is central to our analysis. An angle of  $90^{\circ}$  is typically linked to stratiform clouds, characterized by upward motion in the upper atmosphere and downward motion in the lower atmosphere. Conversely, an angle of  $-90^{\circ}$  suggests a profile associated with shallow convection, where downward motion occurs in the upper atmosphere and upward motion occurs in the lower atmosphere. An angle of  $180^{\circ}$  corresponds to a descending profile without convection, marking regions dominated by subsidence.

Top-heaviness angles between  $\pm 27^{\circ}$  indicate profiles for which the two-mode reconstruction has upward motion at each atmospheric level. We refer to these as "fully ascending" profiles. Marking these boundaries is helpful for analyzing extreme precipitation events where deep convection usually plays a major role. Positive angles from  $0^{\circ}$  to about  $27^{\circ}$  represent fully ascending top-heavy profiles, where the fastest upward motion is in the upper atmosphere. Negative angles from about  $-27^{\circ}$  to  $0^{\circ}$  correspond to fully ascending bottom-heavy profiles, with the fastest upward motion in the lower atmosphere.

#### 4. Two Distinct Modes for Extremes

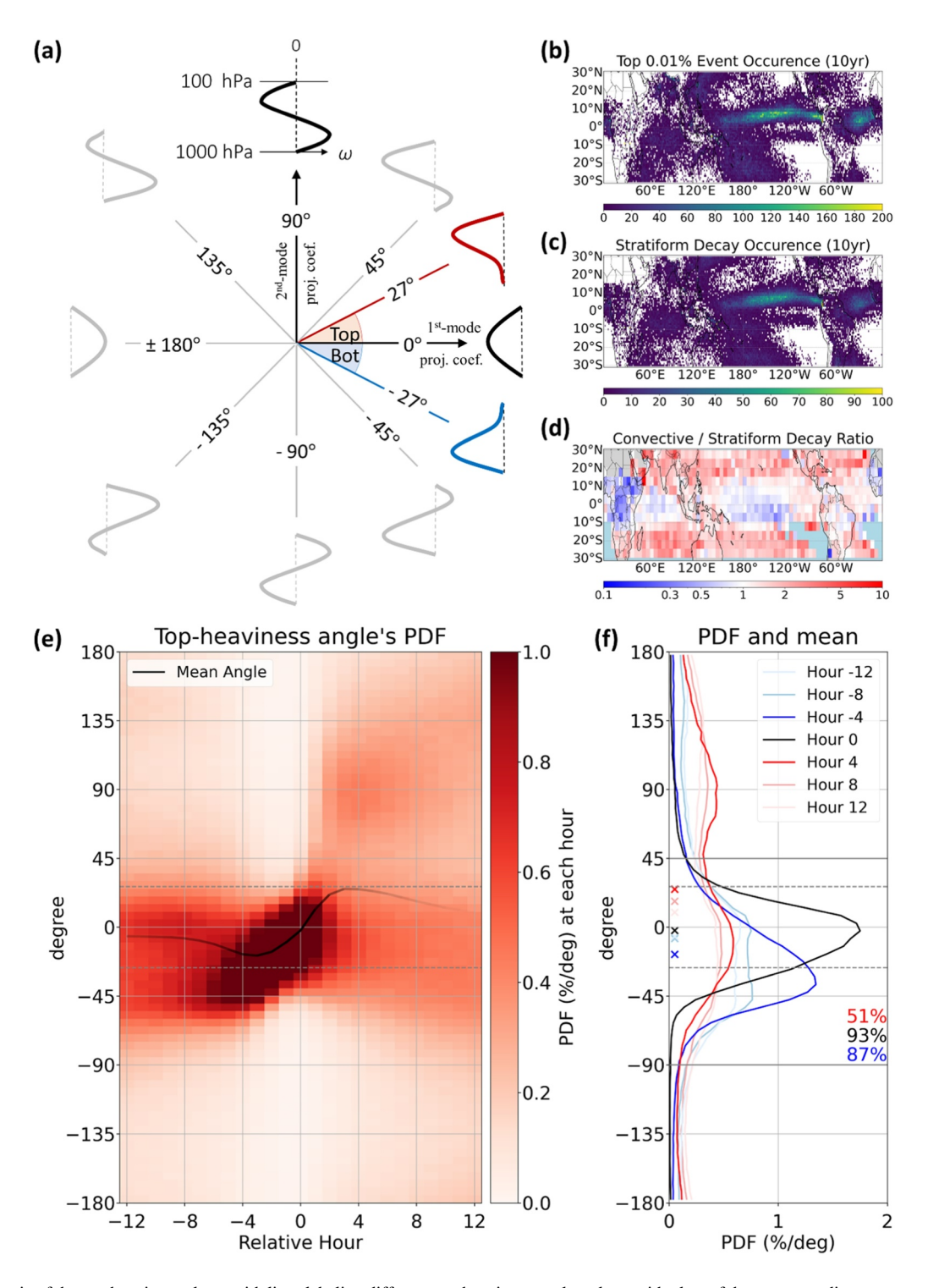
We define precipitation extreme events by identifying individual hours whose precipitation rate exceeds that of all adjacent  $\pm 12$  hr (i.e., each selected hour must be the maximum within a 24-hr window centered on it). We then select the top 0.01% of these peak hours based on their precipitation rate, considering all grid points between 30°N and 30°S in the years 2001–2010. This selection condition guarantees that any two peak hours at the same grid point are at least 13 hr apart, preventing us from counting two peaks that belong to the same 12-hr precipitation burst and thus avoiding double-counting of closely spaced peaks. The peak precipitation threshold for the selected peak hours is 10.58 mm/hr. These extreme events collectively contribute approximately 6.5% of tropical precipitation.

#### 4.1. Bifurcated Regimes After Peak Precipitation

To investigate the evolution of vertical velocity during extreme precipitation events, we analyze the average and probability density function (PDF) of the top-heaviness angle at each hour relative to peak precipitation

LI ET AL. 3 of 13

onlinelibrary.wiley.com/doi/10.1029/2025GL116056 by Hirohiko Masunaga - Nagoya University, Wiley Online Library on [30/10/2025]. See the Terms and Conditions



LI ET AL. 4 of 13

(Figure 1e), where each hour represents the total precipitation accumulated over the preceding hour (i.e., from hour -1 to 0).

The mean angles reveal a transition from a fully ascending bottom-heavy to a fully ascending top-heavy vertical-velocity structure during the 8-hr period centered on peak precipitation. In the four hours leading up to peak precipitation, the PDF of top-heaviness is strongly concentrated around the mean, suggesting most events follow a progression of top-heaviness angle from approximately  $-45^{\circ}-0^{\circ}$ , corresponding to a shift from a bottom-heavy to middle-heavy vertical velocity profile (cf., Figure 1a). However, in the hours after peak precipitation, the PDF becomes bimodal, indicating the existence of two distinct convection modes of top-heaviness angle as the precipitation event decays. At earlier lead times between hours -12 and -8, the PDF also shows a weak visual hint of bimodality. However, the first- and second-mode projection amplitudes at these hours are small (see later discussions in Section 4.3), making the top-heaviness angle highly sensitive to numerical noise.

Focusing on the bimodality post-peak rainfall, we see that the upper branch, with an increasing top-heaviness angle post-peak, transitions from a bottom-heavy to a top-heavy vertical-velocity profile and eventually develops into a stratiform-like profile. We therefore refer to this mode as "stratiform decay." In contrast, the lower branch, with a decreasing top-heaviness angle, has a vertical-velocity profile that remains between bottom-heavy and middle-heavy; we refer to this mode as "convective decay". The distinction between the two main modes becomes clearer when examining the cross sections at specific hours in Figure 1f, which also includes the means for comparison. At hours -4 and 0, the PDFs exhibit a unimodal structure, with over 85% of top-heaviness angles between  $-90^{\circ}$  and  $45^{\circ}$ . From hours -4 to 0, the mode of PDF shifts from -37.5 to  $-2.5^{\circ}$ , accompanied by an increase in the mean top-heaviness angle. At hour 4, the PDF displays a bimodal distribution: 51% of events fall within  $-90^{\circ}$  to  $45^{\circ}$ , while 42% are within  $45^{\circ}-180^{\circ}$ . The increase in the mean angle from hours 0 to 4 reflects a redistribution of vertical motion rather than a simple transition from predominantly bottom-heavy ascent to predominantly top-heavy ascent. That is, rather than a simple shift in the PDF, bottom-heavy profiles diverge into two modes: one into stratiform-like structures with lower-level descent and another into fully ascending topheavy profiles. Together, Figures 1e and 1f illustrate a consistent structural pattern of convection during extreme events, with a unimodal structure before peak precipitation and a bifurcation into two types of convective decay afterward. We therefore define stratiform-decay and convective-decay events based on the top-heaviness angle at hour 4: events with angles from  $45^{\circ}$  to  $180^{\circ}$  are classified as stratiform-decay events, and those from  $-90^{\circ}$ to 45° as convective-decay events. While the threshold choice is somewhat subjective, the PDFs from hours 4 to 12 exhibit a natural minimum near 45°, which separates the two dominant post-peak structures. To ensure a fair and inclusive classification, we defined each mode to span an equal angular range of 135°, which also aligns well with the observed distribution. Sensitivity tests using different classification time points yield similar results (not shown).

#### 4.2. Geographical Distributions

Having defined the two decay types, we now examine the geographical distribution of all extreme events and their decay-type breakdown. The geographical distribution of all the top 0.01% peak hours is shown in Figure 1b, revealing substantial spatial variability. In particular, the eastern ITCZ and tropical Atlantic exhibit high frequencies of extreme precipitation, indicating that the results are largely representative of these regions.

Figure 1c shows the occurrence map of stratiform-decay events, which closely resembles that of all 0.01% extreme events (Figure 1b), with a spatial correlation of 0.818. The map of convective-decay events is also broadly similar (not shown), with a spatial correlation of 0.826 against stratiform-decay events and 0.816 against all extreme events. Although these results suggest that the two decay modes generally coexist across the tropics, the map of the ratio between convective and stratiform-decay events (Figure 1d), regridded to  $5^{\circ} \times 5^{\circ}$  resolution for smoother visualization, reveals regional preferences for one decay mode over the other. In particular, convective-decay events are substantially more common between  $10^{\circ}$  and  $30^{\circ}$  latitude in both hemispheres. One hypothesis is that this latitudinal difference in decay is related to tropical cyclones. We define a TC-related precipitation extreme event as one that occurs within 500 km of a TC center (e.g., Khouakhi et al., 2017), based on the IBTrACS data (Knapp et al., 2010). Within the  $\pm 10^{\circ}$  latitude band, TC-related events and rainfall contribute only 1.20% and 1.51% of the extremes, respectively, whereas in the  $10^{\circ}$ -30° band, they account for 18.34% of events and 25.74% of rainfall. However, while precipitation extremes that are related to tropical

LI ET AL. 5 of 13

cyclones are more likely to be convective-decay events (64.14% of events), even when TC-related events are removed, a similar latitudinal distribution is recovered.

There is also some longitudinal variation in the relative frequency of the two modes in the deep tropics, with the East Pacific showing more stratiform-decay events. This is somewhat different to previous work focused on mean vertical velocity profiles, which find more top-heavy profiles in the in the West versus the East Pacific (Back et al., 2017; Bernardez & Back, 2024). This suggests that extreme events may behave differently from the mean with regards to top-heaviness. Here we continue to focus on precipitation extremes, and we postpone a detailed examination of the relationship between the mean and extremes to future work.

#### 4.3. Distinct Evolution of Vertical Velocity and Precipitation

We now compare the temporal evolution of vertical velocity and precipitation during convective- and stratiformdecay events. Figures 2a and 2b illustrate the composite of intensity projections onto the first and second modes, mapped onto the x and y axes in the top-heaviness plane (cf., Figure 1a). The hours -4 to 4 are highlighted in color, with dashed lines marking the boundaries of fully ascending deep convection at approximately ±27° topheaviness angles. Consistent with Figure 1e, the progression from bottom-heavy to stratiform structures during stratiform-decay events follows an anticlockwise trajectory on the top-heaviness plane, with top-heaviness angles increasing over time (Figure 2a). The convective-decay events also show an anticlockwise trajectory but with only slight increases in top-heaviness angle, from approximately  $-27^{\circ}-0^{\circ}$  (Figure 2b). Convective-decay events are slightly more frequent, comprising 51.1% of all extreme cases compared to 41.2% for stratiform-decay events. One may note that the slight increase in top-heaviness angle after hour 0 in the composites in Figure 2b appears to contradict the decreasing mean top-heaviness angle during convective decay in Figure 1e. However, this discrepancy arises from differences in the averaging procedure. Figure 1e shows the mean top-heaviness angle across events, while the position on the top-heaviness plane plotted in Figure 2b depends additionally on the amplitude of the two modes in each event that contributes to the composite. Points near the origin indicate that vertical velocity projects weakly onto both basis functions, suggesting either weak convective activity or structurally ambiguous profiles. In such cases, the angle alone may not carry clear physical meaning, and caution is warranted in interpreting positions close to the origin.

Importantly, the composites only reflect the average structural tendencies of each decay mode and do not imply that individual events follow a continuous or deterministic trajectory. To assess how persistent each decay type is, we calculate the fraction of events that remain in the same decay category at subsequent hours after the reference point of hour 4. At hour 5, 74.1% of convective-decay events and 69.0% of stratiform-decay events remain in the same category, while at hour 8, the percentages decrease to 59.1% and 48.7%, respectively. These results indicate that transitions between decay types do occur (Masunaga & Takahashi, 2024), but are less common—for example, only 31.3% of convective-decay events switch to stratiform decay at hour 8, while 39.5% of stratiform-decay events switch to convective decay. We speculate that this behavior reflects a form of bistability in convective evolution, whereby convective systems with extreme rainfall may be attracted toward one of two distinct decay regimes but do not always follow a deterministic decay pathway.

In addition to the structural evolution, we also evaluate how well the two-mode decomposition captures the original profiles. The explained variance shown in Figures 2a and 2b indicates the extent to which the first and second modes together can represent the raw vertical velocity profiles. For stratiform-decay events, these two modes explain approximately 89% of the variance at hour -1, above 70% between hours -4 and 1, and above 45% throughout the 24-hr period. For convective-decay events, the explained variance reaches 87% at hour -1, stays above 70% between hours -5 and 2, and exceeds 50% over the full 24 hr. In general, closer to the time of maximum precipitation, both the explained variance and the amplitudes of the two modes increase, indicating that vertical velocity is dominated by these two modes. This demonstrates that the top-heaviness plane is well-suited for analyzing tropical convection, particularly for strong convective events associated with heavy precipitation.

To better visualize changes in the shape and intensity of vertical velocity, Figures 2c and 2d present the composite raw vertical velocity profiles alongside those reconstructed by the two modes, illustrating the transitions in convection before the peak (in blue) and after the peak (in red). The maximum upward vertical velocity across the vertical profile occurs at hour 1 throughout the time series for both decay events, with stratiform decay exhibiting larger magnitude velocities in both the raw and reconstructed profiles. For stratiform-decay events, the profiles transition from bottom-heavy to middle-heavy, then top-heavy, and ultimately evolve into a stratiform-like

LI ET AL. 6 of 13

19448007, 2025, 21, Downloaded from https://agupubs.onlinelibrary.wiley.com/doi/10.1029/2025GL116056 by Hirohiko Masunaga - Nagoya University , Wiley Online Library on [30/10/2025]. See the Terms and Conditions

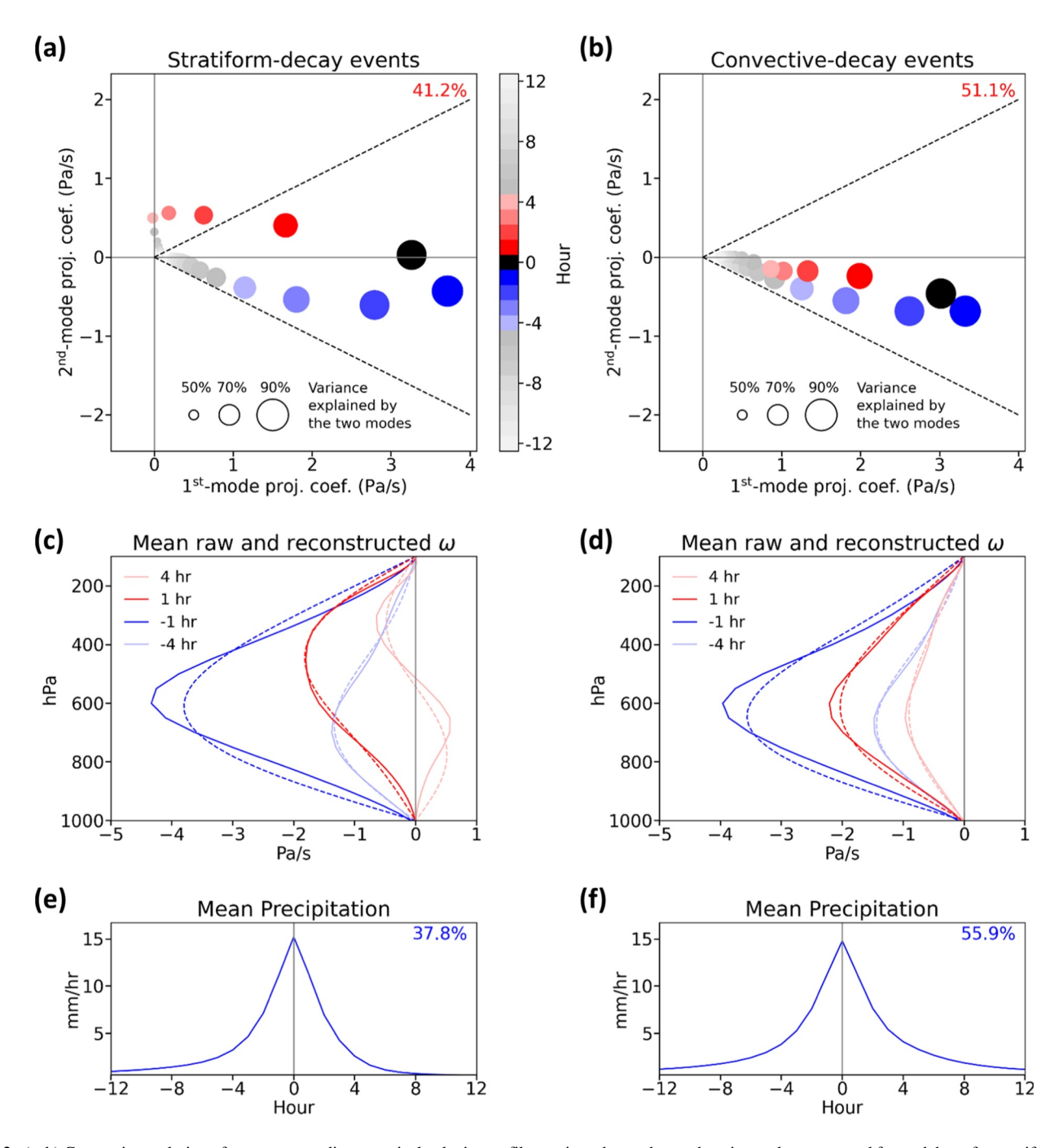


**Figure 2.** (a, b) Composite evolution of pressure-coordinate vertical velocity profiles projected onto the top-heaviness plane averaged for each hour for stratiform-decay (a) and convective-decay events (b). The *x*-axis represents projection coefficient of the first baroclinic mode, and the *y*-axis represents that of the second baroclinic mode (details in Section 3). Point sizes represent the variance explained by the two modes, with dashed lines marking the boundaries for fully ascending profiles. (c, d) Mean raw pressure-coordinate vertical velocity profiles (solid) and the two-mode reconstructed profiles (dashed) for the selected hours of stratiform-decay events (c) and convective-decay events (d). (e, f) Mean precipitation rate for stratiform-decay events (e) and convective-decay events (f). The percentage indicates the total contribution of the 24-hr rainfall to the total extreme events.

structure (Figure 2c). In contrast, the profiles for convective-decay events maintain a fully ascending relatively bottom-heavy shape, with changes primarily restricted to the intensity (Figure 2d). These characteristics are consistent with the patterns observed in Figures 2a and 2b, respectively.

For both stratiform- and convective-decay events, the precipitation rate peaks sharply near hour 0, reaching approximately 15 mm per hour (Figures 2e and 2f). However, their subsequent evolution diverges. Precipitation

LI ET AL. 7 of 13

during stratiform-decay events declines rapidly with an e-folding time of approximately 2.5 hr, nearly ceasing after hour 8 (Figure 2e), while convective-decay events exhibit a longer tail with an e-folding time of about 3 hr, sustaining precipitation over a more extended period (Figure 2f). This prolonged precipitation, combined with the higher frequency, results in convective-decay events contributing 55.9% of the total precipitation during extreme events, compared to the 37.8% contribution from stratiform-decay events. The remaining 6.3% of precipitation corresponds to events with top-heaviness angles within the range of  $(-180^{\circ}, -90^{\circ})$  at hour 4, lying outside the prescribed classification range of  $-90^{\circ}-180^{\circ}$ . We note that previous studies have highlighted the dominant role of MCSs in the tropics, with MCSs accounting for more than half of the total tropical precipitation (e.g., Feng et al., 2021). While our analysis does not apply any object-based algorithm and focuses exclusively on extreme rainfall events, the substantial contribution from convective-decay events reported here may reflect the convective cores embedded within MCSs. In addition to our preliminary investigation of tropical cyclone–related events, extending the current framework to include MCSs—through object-based classification—would be a valuable direction for future work.

Traditionally, tropical deep convection has been assumed to mainly decay into stratiform precipitation, a pathway considered canonical (Benedict & Randall, 2007; Houze, 1997). However, our analysis identifies a distinct convective-decay mode that complements this perspective. This mode appears to exert a greater influence on short-duration heavy precipitation events, underscoring the need to revisit convection decay processes and their implications for precipitation dynamics, especially at the sub-daily scale.

#### 4.4. Association With Environmental Buoyancy, Instability and Moisture

With the two modes of convection evolution identified, an essential question arises: what environmental factors lead convection to follow one mode instead of the other? We begin by analyzing the lower-free-tropospheric plume buoyancy,  $B_L$ . Introduced by Ahmed and Neelin (2018) and simplified in Ahmed et al. (2020),  $B_L$  approximates the mid-tropospheric buoyancy of a rising plume that mixes with its lower-tropospheric environment. Combining measures of convective instability and tropospheric moisture, the plume buoyancy has been shown to be a predictor of precipitation over tropical ocean and land.  $B_L$  is expressed as:

$$B_L = g \left[ w_B \frac{\theta_{eB} - \theta_{eL}^*}{\theta_{eI}^*} - w_L \frac{\theta_{eL}^+}{\theta_{eI}^*} \right], \tag{3}$$

where g is acceleration due to gravity,  $\theta_{eB}$  the boundary-layer-averaged equivalent potential temperature,  $\theta_{eL}^*$  the lower-free-tropospheric-averaged saturated equivalent potential temperature, and  $\theta_{eL}^+ = \theta_{eL}^* - \theta_{eL}$  is a measure of subsaturation, where  $\theta_{eL}$  is the lower-free-tropospheric-averaged equivalent potential temperature. The parameters  $w_B$  and  $w_L$  represent the relative influence of the boundary layer and lower-free-troposphere layers on the composition of the air parcel, respectively. They are defined following Ahmed and Neelin (2018) and simplified in Adames et al., 2021, consistent with a "deep" inflow profile,

$$w_B = \frac{\Delta p_B}{\Delta p_L} \ln \left( 1 + \frac{\Delta p_L}{\Delta p_B} \right),\tag{4}$$

$$w_L = 1 - w_R. (5)$$

Here,  $\Delta p_B$  and  $\Delta p_L$  are the pressure thicknesses in the boundary layer and the lower free troposphere, respectively.

In this study we compute  $B_L$  and its undiluted component (given by the first term in Equation 3), which serves as a CAPE-like measure of atmospheric instability. Following Adames et al. (2021), we use  $\Delta p_B = 150$  and  $\Delta p_L = 250$  hPa to yield  $w_B = 0.59$ , and we take quantities defined in the boundary layer and free troposphere as averages between pressure levels of 1,000 and 850 hPa and 850 and 600 hPa, respectively. While, in principle, the top-heaviness of a given profile could be used to modify the inflow assumptions, for simplicity, we use fixed  $\Delta p_B$  and  $\Delta p_L$  in Equation 4 for all profiles.

Figures 3a and 3b illustrate the temporal evolution of mean  $B_L$  (solid line) and its undiluted component (dashed line). Both measurements reach a maximum at hours -2 or -1 in both decay modes, consistent with the observation that the maximum precipitation rate lags maximum buoyancy (Adames et al., 2021; Wolding

LI ET AL. 8 of 13

onlinelibrary.wiley.com/doi/10.1029/2025GL116056 by Hirohiko Masunaga - Nagoya University , Wiley Online Library on [30/10/2025]. See the Terms a

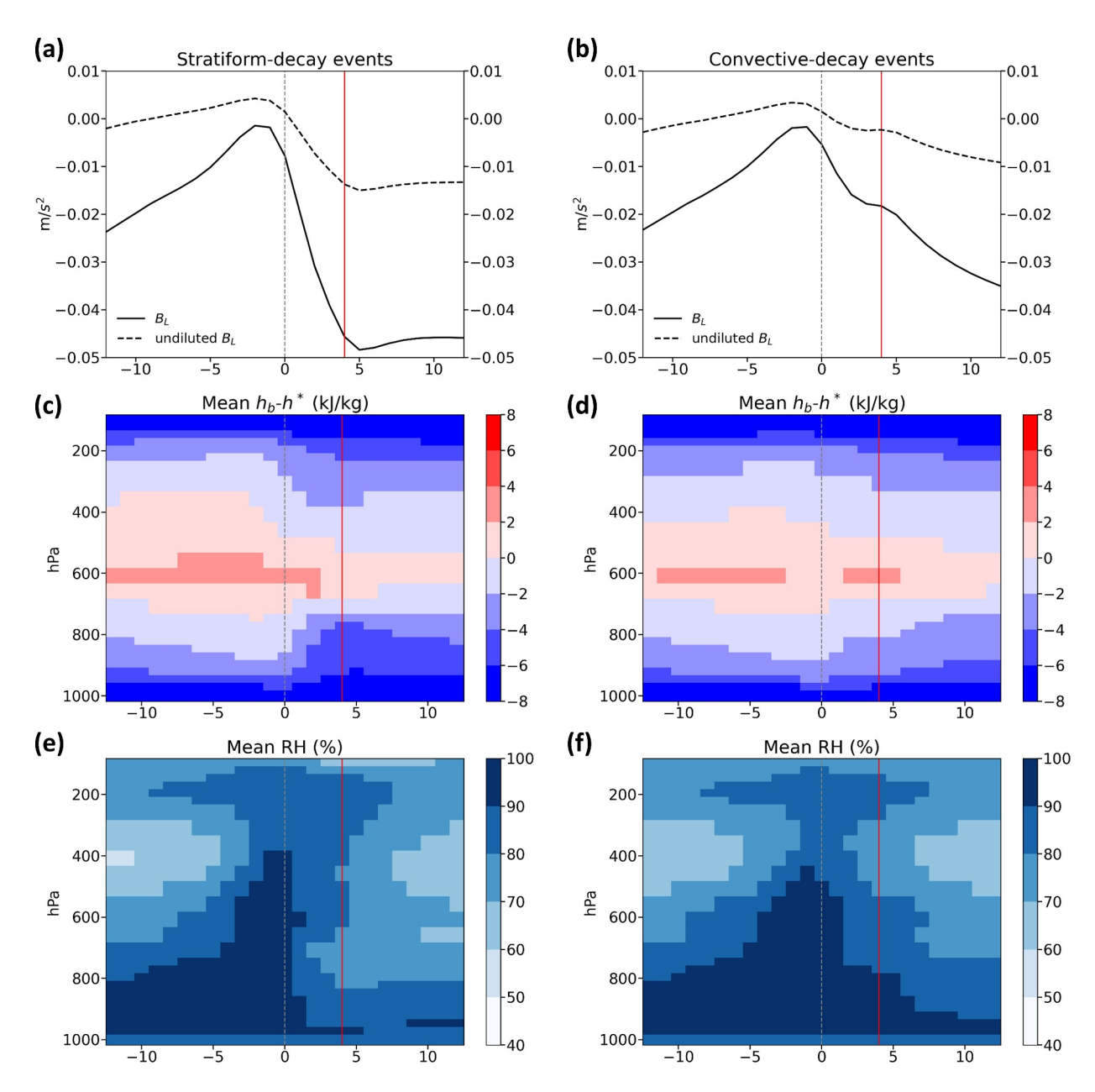


Figure 3. (a, b) Evolution of mean lower-tropospheric plume buoyancy ( $B_L$ , solid line) and its undiluted component (dashed line) for the stratiform-decay (a) and convective-decay events (b). (c, d) Composite instability, shown as the difference between boundary-layer (850–1,000 hPa) averaged moist static energy ( $h_b$ ) and saturation moist static energy ( $h^*$ ) for the stratiform-decay (c) and convective-decay events (d). (e, f) Mean relative humidity profile in percentage for the stratiform-decay (e) and convective-decay events (f). In all panels, the red line at hour 4 marks the time classifying stratiform-decay and convective-decay events.

et al., 2022). Although their evolutions appear similar for both modes prior to peak precipitation,  $B_L$  and its undiluted component drop much more rapidly, reaching values lower than those before peak precipitation for stratiform-decay events (Figure 3a) soon afterward. For convective-decay events, the drop is more gradual, with buoyancy at hour 4 (red line) remaining higher than that at hour -12 (Figure 3b). The difference between  $B_L$  and the undiluted  $B_L$ , reflecting the subsaturation of the lower atmosphere, increases after the peak precipitation in both modes, with stratiform-decay events showing a larger disparity. This larger disparity, combined with the greater drop in  $B_L$  values, suggests that although atmospheric conditions in both decay events become more stable and drier after the peak hour, stratiform decay undergoes greater stabilization and drying than convective decay.

LI ET AL. 9 of 13

To explore the vertical structure rather than layer-integrated averages of the atmosphere, we examine the temporal changes of profiles of instability and moisture. Figures 3c and 3d show the vertical distribution of instability for undiluted air parcels, defined as the moist static energy averaged over the boundary layer  $(h_b)$  minus the saturation moist static energy  $(h^*)$  at each level. In both modes, the instability generally increases before the peak precipitation and decreases afterward, consistent with the evolution of undiluted  $B_L$  (Figures 3a and 3b). Also, the minimum of the lowest instability aggregated over the vertical aligns with the minimum of undiluted  $B_L$ : occurring at hour 5 for stratiform-decay events, while delayed until hour 12 for convective-decay events. Driven by stronger negative instability below 700 hPa, the lower atmosphere during stratiform decay becomes more stable, creating an environment less favorable for maintaining deep convection (Figure 3c). As convection may dissipate more quickly under such a condition, this stabilization is likely associated with the sooner decline of post-peak precipitation during stratiform decay (Figure 2e).

We now turn to the moisture distribution and examine the vertical profile of subsaturation. Figures 3e and 3f present the temporal evolution of relative humidity profiles. In both modes, the relative humidity at all levels increases when approaching peak precipitation consistent with findings of previous studies (e.g., Holloway & Neelin, 2009; Masunaga, 2012; Sherwood & Wahrlich, 1999). After peak precipitation, moisture declines sharply for stratiform-decay events (Figure 3e), while the decrease is more gradual for convective-decay events (Figure 3f). The distinct differences in lower atmospheric humidity and instability suggest that convection during stratiform decay likely experiences a less favorable environment, leading to a faster dissipation compared to convective decay. Additionally, the upper atmospheric humidity, particularly between 300 and 550 hPa, is generally higher for stratiform-decay events after peak precipitation, potentially related to the stratiform structures of vertical velocity.

Overall, Figure 3 suggests that a lower atmosphere characterized by reduced buoyancy, instability, and humidity—indicative of a stable and dry environment—may accelerate the cessation of rainfall by inhibiting convection for stratiform-decay events. However, none of these indicators is predictive; it is only after the peak precipitation that their differences can be observed. That is, one can't determine whether convection will follow one mode or the other based solely on environmental thermodynamic parameters. The causal relationship between convective dynamics and the thermodynamic environment also remains unclear. That is, it is unclear whether changes in the thermodynamic environment drive the differences in vertical velocity profiles between convective decay and stratiform decay events or rather it is the differences in the vertical velocity profile that result in differences in the environment. For example, humidity in the lower troposphere is increased by strong bottom-heavy upward motion. Thus, the more gradual reduction in humidity in the convective-decay cases may be a result of the maintenance of a bottom-heavy vertical velocity profile rather than a cause. These remaining challenges highlight the need for more detailed dynamical analyses to uncover the mechanisms at play around the peak precipitation.

Finally, to test the robustness of our results, we repeated our analysis using the Modern-Era Retrospective Analysis for Research and Applications, Version 2 (MERRA-2; Gelaro et al., 2017), with its 3-hourly  $0.5^{\circ} \times 0.625^{\circ}$  resolution. The two distinct modes with similar features are also identified, despite higher buoyancy, instability, moisture, and precipitation in MERRA-2 compared to ERA-5 (not shown). In addition, we repeated the analysis using ERA5 data coarsened to  $1^{\circ}$  resolution using conservative regridding (for the year 2001), and again found consistent bi-modal evolution (not shown). This cross-dataset and cross-resolution agreement gives us confidence that our conclusions reflect large-scale dynamics rather than artifacts associated with a particular data set or spatial resolution. We also considered different regions of analysis; results for the region between  $\pm 10^{\circ}$  or  $\pm 20^{\circ}$  are similar to the region between  $\pm 30^{\circ}$  shown here, and considering ocean-only points also produces qualitatively similar results, matching the expectation that extreme events are concentrated in the deep tropics and over oceans (Lv et al., 2023; Roca & Fiolleau, 2020).

#### 5. Concluding Remarks

By projecting vertical velocity profiles onto the two basis functions representing the prevailing vertical modes of vertical velocity in the tropics, we construct a two-dimensional top-heaviness plane to diagnose the evolution of vertical velocity in precipitation events. We have shown that the top-heaviness plane demonstrates a strong capacity to distill the multi-dimensional vertical velocity profiles into a two-dimensional visual representation, effectively capturing the dominant patterns of ascent and descent.

LI ET AL. 10 of 13

Applying the top-heaviness plane to tropical precipitation extreme events, we identify two distinct modes on the evolution of the vertical velocity profile after peak precipitation—stratiform decay and convective decay. Stratiform-decay events transition rapidly through bottom-heavy, top-heavy, and stratiform-like vertical velocity profiles and are associated with sharp reductions in plume buoyancy, instability, and moisture, particularly in the lower atmosphere. This evolution creates a stable, dry environment, halting rainfall approximately 8 hr after the precipitation peak. In contrast, convective-decay events consistently sustain bottom-heavy structures in the vertical velocity profile with a slower post-peak decline in plume buoyancy and moisture, allowing precipitation to persist beyond 12 hr. The higher frequency of convective-decay events and their extended duration of precipitation result in a larger share of total rainfall during extreme events compared to stratiform-decay events.

Previous studies of the life cycles of tropical convective events have highlighted transitions from shallow convection to deep convection and eventually stratiform cloud distributions (e.g., Mapes & Houze, 1995). These transitions have been related to the structure of MCSs (e.g., Houze, 1997) and correspond well to our stratiform decay mode. However, our analysis shows that the convective decay mode accounts for the larger fraction of tropical precipitation extremes, suggesting a different perspective on the dominant dynamics of tropical precipitation extreme events. This post-peak bifurcation may reflect differing discharge behavior of lower-tropospheric buoyancy, similar to distinct transitions between deep-to-shallow and deep-to-deep convective regimes (Wolding et al., 2024), although this analogy should be interpreted with caution given the transitions in Wolding et al. (2024) were defined in daily timescales.

Nonetheless, puzzles remain. Prior to peak precipitation, minimal thermodynamic environmental differences suggest that convection abruptly diverges into distinct modes, with no clear early warning signals. However, we have not examined potential dynamical precursors, such as vertical wind shear, which may play a role in shaping the convective evolution. Also, tropical cyclones contribute disproportionately to convective-decay events, suggesting that convective system movement may influence the observed decay modes. Eulerian composites alone may not fully disentangle intrinsic evolution from the effects of advection. Future studies should explore the mechanisms underlying this sudden transition around the peak precipitation, and examine decay modes from a Lagrangian perspective to better isolate system-scale evolution.

To assess the robustness of these conclusions to the choice of reference precipitation, we repeated the full eventselection and composite analysis with IMERG (2007-2009, 0.1° raw resolution). The hallmark transition from a single-to a double-peaked top-heaviness PDF, while weaker, remains present when using IMERG, confirming that it is not an artefact of ERA5 (not shown). Given spatial mismatches between IMERG and ERA5 in locating extreme rainfall, which likely weakens the captured dynamical signal in ERA5 composites, we retain ERA5 throughout the manuscript to ensure internal consistency. However, since vertical velocity is not directly observed in the atmosphere, our results are dependent on the fidelity of the underlying model used to produce these data sets. The vertical velocity is known to be influenced by unresolved processes such as convection, and this represents a key uncertainty in our results. The disagreement between reanalyzes and observations is especially pronounced in oceanic regions, where fields are largely governed by model physics (Hagos et al., 2010; Huaman et al., 2022). An alternative approach would be to apply the top-heaviness plane framework to more direct observations of vertical velocity. This might include single-site measurements (e.g., Kumar et al., 2015), although these measurements provide velocity profiles at a smaller scale than those of reanalysis. Field campaign measurements, in which the large-scale vertical motion is constrained through multiple soundings, could also be used to investigate top-heaviness in observations (e.g., Bony & Stevens, 2019). However, such observations are unlikely to have sufficient time resolution for the analysis performed here. Given the limitations of observations of vertical velocity, a promising direction is to investigate the evolution of vertical cloud patterns using satellite products to explore potential differences from the two modes identified in this study.

Finally, an important direction for future work is to investigate more deeply the geographic variations of topheaviness evolution across the tropics. As pointed out in relation to Figure 1d, the top-heaviness in extreme precipitation has a different spatial structure from that of the mean. Here, we find the eastern Pacific to be dominated by stratiform decay, indicating greater top-heaviness, whereas previous work has found higher topheaviness of the mean vertical motion in the western Pacific than in the east (Back et al., 2017; Bernardez & Back, 2024). The extent to which these differences can be understood by examining the different modes of discrete convective events as defined in this paper remains an open question. Another aspect to explore is whether the two modes tend to be associated with large-scale or small-scale systems and whether they are more commonly

LI ET AL. 11 of 13

Acknowledgments

MSS and YXL acknowledge support from

the Centre of Excellence for the Weather of

was supported by the National Science and

the Australian Research Council through

the 21st Century (CE230100012) and

Grant DP230102077, respectively. JYY

Technology Council in Taiwan through

Grant NSTC113-2111-M008-032. This

assistance of resources from the National

Australia), an NCRIS enabled capability

supported by the Australian Government.

Steven Sherwood for his valuable insights

Brandon Wolding and Professor Larissa Back for their thoughtful and constructive

reviews, which significantly improved the

quality and clarity of the manuscript. Open

access publishing facilitated by Monash

University agreement via the Council of

Australian University Librarians.

University, as part of the Wiley - Monash

We express our gratitude to Professor

and discussions. We also thank Dr.

research was undertaken with the

Computational Infrastructure (NCI

linked to moving or localized convection. The land-sea contrast is also a potential avenue for investigation, particularly in the context of extreme events over land, which can lead to more severe and destructive impacts on human populations (e.g., Prein et al., 2023).

#### **Conflict of Interest**

The authors declare no conflicts of interest relevant to this study.

#### **Data Availability Statement**

The ERA5 reanalysis products used in this study were obtained from the Copernicus Climate Data Store (Hersbach et al., 2020). The single-level data are available at <a href="https://cds.climate.copernicus.eu/datasets/reanalysis-era5-single-levels">https://cds.climate.copernicus.eu/datasets/reanalysis-era5-single-levels</a>, and the pressure-level data are available at <a href="https://cds.climate.copernicus.eu/datasets/reanalysis-era5-pressure-levels">https://cds.climate.copernicus.eu/datasets/reanalysis-era5-pressure-levels</a>. The MERRA-2 3D Instantaneous 3-hourly Assimilation (inst3\_3d\_asm\_Np) data set, used for robustness testing in this work, is accessible at <a href="https://doi.org/10.5067/QBZ6MG944HW0">https://doi.org/10.5067/QBZ6MG944HW0</a>. The International Best Track Archive for Climate Stewardship (IBTrACS) data (Knapp et al., 2010), used to identify tropical cyclone–related events, is available at <a href="https://www.ncei.noaa.gov/products/international-best-track-archive">https://www.ncei.noaa.gov/products/international-best-track-archive</a>. The Python code used for the vertical-motion projection (top-heaviness) is publicly available and archived on Zenodo at <a href="https://doi.org/10.5281/zenodo.17358494">https://doi.org/10.5281/zenodo.17358494</a> (Li, 2025).

#### References

Adames, Á. F., Powell, S. W., Ahmed, F., Mayta, V. C., & Neelin, J. D. (2021). Tropical precipitation evolution in a buoyancy-budget framework. Journal of the Atmospheric Sciences, 78(2), 509–528. https://doi.org/10.1175/JAS-D-20-0074.1

Ahmed, F., Adames, Á. F., & Neelin, J. D. (2020). Deep convective adjustment of temperature and moisture. *Journal of the Atmospheric Sciences*, 77(6), 2163–2186. https://doi.org/10.1175/JAS-D-19-0227.1

Ahmed, F., & Neelin, J. D. (2018). Reverse engineering the tropical precipitation–buoyancy relationship. *Journal of the Atmospheric Sciences*, 75(5), 1587–1608. https://doi.org/10.1175/JAS-D-17-0333.1

Back, L. E., & Bretherton, C. S. (2006). Geographic variability in the export of moist static energy and vertical motion profiles in the tropical Pacific. *Geophysical Research Letters*, 33(17), L17810. https://doi.org/10.1029/2006GL026672

Back, L. E., & Bretherton, C. S. (2009). A simple model of climatological rainfall and vertical motion patterns over the tropical oceans. *Journal of Climate*, 22(23), 6477–6497. https://doi.org/10.1175/2009JCLI2393.1

Back, L. E., Hansen, Z., & Handlos, Z. (2017). Estimating vertical motion profile top-heaviness: Reanalysis compared to satellite-based observations and stratiform rain fraction. *Journal of the Atmospheric Sciences*, 74(3), 855–864. https://doi.org/10.1175/JAS-D-16-0062.1

Benedict, J. J., & Randall, D. A. (2007). Observed characteristics of the MJO relative to maximum rainfall. *Journal of the Atmospheric Sciences*, 64(7), 2332–2354. https://doi.org/10.1175/JAS3968.1

Bernardez, M., & Back, L. (2024). Integrating thermodynamic and dynamic views on the control of the top-heaviness of convection in the Pacific ITCZ with weak temperature gradient simulations. *Journal of Advances in Modeling Earth Systems*, 16(2), e2022MS003455. https://doi.org/10.

Bony, S., & Stevens, B. (2019). Measuring area-averaged vertical motions with dropsondes. *Journal of the Atmospheric Sciences*, 76(3), 767–783. https://doi.org/10.1175/JAS-D-18-0141.1

Chen, Y.-C., & Yu, J.-Y. (2021). Modes of tropical convection and their roles in transporting moisture and moist static energy: Contrast between deep and shallow convection. Climate Dynamics, 57(5), 1789–1803. https://doi.org/10.1007/s00382-021-05777-x

Feng, Z., Leung, L. R., Liu, N., Wang, J., Houze, R. A., Li, J., et al. (2021). A global high-resolution mesoscale convective system database using satellite-derived cloud tops, surface precipitation, and tracking. *Journal of Geophysical Research: Atmospheres*, 126(8), e2020JD034202. https://doi.org/10.1029/2020JD034202

Gelaro, R., McCarty, W., Suárez, M. J., Todling, R., Molod, A., Takacs, L., et al. (2017). The modern-era retrospective analysis for research and applications, version 2 (MERRA-2) [Dataset]. *Journal of Climate*, 30(14), 5419–5454. https://doi.org/10.1175/jcli-d-16-0758.1

Gu, L., Yin, J., Gentine, P., Wang, H. M., Slater, L. J., Sullivan, S. C., et al. (2023). Large anomalies in future extreme precipitation sensitivity driven by atmospheric dynamics. *Nature Communications*, 14(1), 3197. https://doi.org/10.1038/s41467-023-39039-7

Hagos, S., Zhang, C., Tao, W.-K., Lang, S., Takayabu, Y. N., Shige, S., et al. (2010). Estimates of tropical diabatic heating profiles: Commonalities and uncertainties. *Journal of Climate*, 23(3), 542–558. https://doi.org/10.1175/2009JCLI3025.1

Hersbach, H., Bell, B., Berrisford, P., Hirahara, S., Horányi, A., Muñoz-Sabater, J., et al. (2020). The ERA5 global reanalysis [Dataset]. Quarterly Journal of the Royal Meteorological Society, 146(730), 1999–2049. https://doi.org/10.1002/qj.3803

Holloway, C. E., & Neelin, J. D. (2009). Moisture vertical structure, column water vapor, and tropical deep convection. *Journal of the Atmospheric Sciences*, 66(6), 1665–1683. https://doi.org/10.1175/2008JAS2806.1

Houze, R. A. J. (1997). Stratiform precipitation in regions of convection: A meteorological paradox? Bulletin of the American Meteorological Society, 78(10), 2179–2195. https://doi.org/10.1175/1520-0477(1997)078<2179:spiroc>2.0.co;2

Huaman, L., Schumacher, C., & Sobel, A. H. (2022). Assessing the vertical velocity of the East Pacific ITCZ. Geophysical Research Letters, 49(1), e2021GL096192. https://doi.org/10.1029/2021GL096192

Inoue, K., Adames, Á. F., & Yasunaga, K. (2020). Vertical velocity profiles in convectively coupled equatorial waves and MJO: New diagnoses of vertical velocity profiles in the wavenumber–frequency domain. *Journal of the Atmospheric Sciences*, 77(6), 2139–2162. https://doi.org/10. 1175/JAS-D-19-0209.1

Inoue, K., & Back, L. E. (2015a). Column-integrated moist static energy budget analysis on various time scales during TOGA COARE. *Journal of the Atmospheric Sciences*, 72(5), 1856–1871. https://doi.org/10.1175/JAS-D-14-0249.1

LI ET AL. 12 of 13



### **Geophysical Research Letters**

- 10.1029/2025GL116056
- Inoue, K., & Back, L. E. (2015b). Gross moist stability assessment during TOGA COARE: Various interpretations of gross moist stability. Journal of the Atmospheric Sciences, 72(11), 4148–4166. https://doi.org/10.1175/JAS-D-15-0092.1
- Inoue, K., & Back, L. E. (2017). Gross moist stability analysis: Assessment of satellite-based products in the GMS plane. Journal of the Atmospheric Sciences, 74(6), 1819–1837. https://doi.org/10.1175/JAS-D-16-0218.1
- Johnson, R. H., Rickenbach, T. M., Rutledge, S. A., Ciesielski, P. E., & Schubert, W. H. (1999). Trimodal characteristics of Tropical convection. Journal of Climate, 12(8), 2397–2418. https://doi.org/10.1175/1520-0442(1999)012<2397:tcotc>2.0.co;2
- Khouakhi, A., Villarini, G., & Vecchi, G. A. (2017). Contribution of tropical cyclones to rainfall at the global scale. *Journal of Climate*, 30(1), 359–372. https://doi.org/10.1175/JCLI-D-16-0298.1
- Kiladis, G. N., Wheeler, M. C., Haertel, P. T., Straub, K. H., & Roundy, P. E. (2009). Convectively coupled equatorial waves. Reviews of Geophysics, 47(2), RG2003. https://doi.org/10.1029/2008RG000266
- Knapp, K. R., Kruk, M. C., Levinson, D. H., Diamond, H. J., & Neumann, C. J. (2010). The international best track archive for climate stewardship (IBTrACS) [Dataset]. Bulletin of the American Meteorological Society, 91(3), 363–376. https://doi.org/10.1175/2009BAMS2755.1
- Kumar, V. V., Jakob, C., Protat, A., Williams, C. R., & May, P. T. (2015). Mass-flux characteristics of tropical cumulus clouds from wind profiler observations at Darwin, Australia. *Journal of the Atmospheric Sciences*, 72(5), 1837–1855. https://doi.org/10.1175/JAS-D-14-0259.1
- Lee, D., Oreopoulos, L., Huffman, G. J., Rossow, W. B., & Kang, I.-S. (2013). The precipitation characteristics of ISCCP tropical weather states. Journal of Climate, 26(2), 772–788. https://doi.org/10.1175/JCLI-D-11-00718.1
- Li, Y.-X., Masunaga, H., Takahashi, H., & Yu, J.-Y. (2024). When, where and to what extent do temperature perturbations near tropical deep convection follow convective quasi equilibrium? *Geophysical Research Letters*, 51(11), e2024GL108233. https://doi.org/10.1029/2024GL108233
- Li, Y.-X. (2025). Python code for vertical-motion projection (top-heaviness) [Software]. Zenodo. https://doi.org/10.5281/zenodo.17358494
- Lin, J., Mapes, B., Zhang, M., & Newman, M. (2004). Stratiform precipitation, vertical heating profiles, and the Madden–Julian oscillation. Journal of the Atmospheric Sciences, 61(3), 296–309. https://doi.org/10.1175/1520-0469(2004)061<0296:SPVHPA>2.0.CO;2
- Lv, P., Hao, H., & Wu, G. (2023). Differences in global precipitation regimes between land and ocean areas based on the GPM IMERG product. *Remote Sensing*, 15(17), 4179. https://doi.org/10.3390/rs15174179
- Mapes, B., Tulich, S., Lin, J., & Zuidema, P. (2006). The mesoscale convection life cycle: Building block or prototype for large-scale tropical waves? *Dynamics of Atmospheres and Oceans*, 42(1–4), 3–29. https://doi.org/10.1016/j.dynatmoce.2006.03.003
- Mapes, B. E., & Houze, R. A., Jr. (1995). Diabatic divergence profiles in western Pacific mesoscale convective systems. *Journal of the Atmospheric Sciences*, 52(10), 1807–1828. https://doi.org/10.1175/1520-0469(1995)052<1807:DDPIWP>2.0.CO;2
- Masunaga, H. (2012). A satellite study of the atmospheric forcing and response to moist convection over tropical and subtropical oceans. *Journal of the Atmospheric Sciences*, 69(1), 150–167. https://doi.org/10.1175/JAS-D-11-016.1
- Masunaga, H., & L'Ecuyer, T. S. (2014). A mechanism of tropical convection inferred from observed variability in the moist static energy budget. Journal of the Atmospheric Sciences, 71(10), 3747–3766. https://doi.org/10.1175/JAS-D-14-0015.1
- Masunaga, H., & Takahashi, H. (2024). The energetics of the Lagrangian evolution of tropical convective systems. *Journal of the Atmospheric Sciences*, 81(4), 783–799. https://doi.org/10.1175/JAS-D-23-0141.1
- Neogi, S., & Singh, M. S. (2022). Understanding changes in the tropical circulation under global warming using a cloud-resolving model and a conceptual model. *Journal of Climate*, 35(18), 5855–5868. https://doi.org/10.1175/JCLI-D-21-0854.1
- O'Gorman, P. A., & Schneider, T. (2009a). Scaling of precipitation extremes over a wide range of climates simulated with an idealized GCM. Journal of Climate, 22(21), 5676–5685. https://doi.org/10.1175/2009JCLI2701.1
- O'Gorman, P. A., & Schneider, T. (2009b). The physical basis for increases in precipitation extremes in simulations of 21st-century climate change. *Proceedings of the National Academy of Sciences*, 106(35), 14773–14777. https://doi.org/10.1073/pnas.0907610106
- Prein, A. F., Mooney, P. A., & Done, J. M. (2023). The multi-scale interactions of atmospheric phenomenon in mean and extreme precipitation. Earth's Future, 11(11), e2023EF003534. https://doi.org/10.1029/2023EF003534
- Riley, E. M., Mapes, B. E., & Tulich, S. N. (2011). Clouds associated with the Madden-Julian Oscillation: A new perspective from Cloudsat. Journal of the Atmospheric Sciences, 68(12), 3032–3051. https://doi.org/10.1175/JAS-D-11-030.1
- Roca, R., & Fiolleau, T. (2020). Extreme precipitation in the tropics is closely associated with long-lived convective systems. Communications Earth & Environment, 1(1), 18. https://doi.org/10.1038/s43247-020-00015-4
- Rossow, W. B., Mekonnen, A., Pearl, C., & Goncalves, W. (2013). Tropical precipitation extremes. *Journal of Climate*, 26(5), 1457–1466. https://doi.org/10.1175/JCLI-D-11-00725.1
- Sherwood, S. C., & Wahrlich, R. (1999). Observed evolution of tropical deep convective events and their environment. *Monthly Weather Review*, 127(8), 1777–1795. https://doi.org/10.1175/1520-0493(1999)127<1777:OEOTDC>2.0.CO;2
- Singh, M. S., & Neogi, S. (2022). On the interaction between moist convection and large-scale ascent in the tropics. *Journal of Climate*, 35(14), 4417–4435. https://doi.org/10.1175/JCLI-D-21-0717.1
- Sobel, A. H., Nilsson, J., & Polvani, L. M. (2001). The weak temperature gradient approximation and balanced tropical moisture waves. *Journal of the Atmospheric Sciences*, 58(23), 3650–3665. https://doi.org/10.1175/1520-0469(2001)058\3650:TWTGAA\2.0.CO;2
- Takayabu, Y. N., Lau, K.-M., & Sui, C.-H. (1996). Observation of a quasi-2-day wave during TOGA COARE. *Monthly Weather Review*, 124(9), 1892–1913. https://doi.org/10.1175/1520-0493(1996)124<1892:OOAQDW>2.0.CO;2
- Tan, J., Jakob, C., Rossow, W. B., & Tselioudis, G. (2015). Increases in tropical rainfall driven by changes in frequency of organized deep convection. *Nature*, 519(7544), 451–454. https://doi.org/10.1038/nature14339
- Tsai, Y.-C., & Yu, J.-Y. (2023). Contrasting the energy recharge-discharge cycle between propagating and eastward-decaying Madden–Julian oscillation events. *Climate Dynamics*, 61(7), 2565–2579. https://doi.org/10.1007/s00382-023-06711-z
- Wolding, B., Powell, S. W., Ahmed, F., Dias, J., Gehne, M., Kiladis, G., & Neelin, J. D. (2022). Tropical thermodynamic–convection coupling in observations and reanalyses. *Journal of the Atmospheric Sciences*, 79(7), 1781–1803. https://doi.org/10.1175/JAS-D-21-0256.1
- Wolding, B., Rydbeck, A., Dias, J., Ahmed, F., Gehne, M., Kiladis, G., et al. (2024). Atmosphere–Ocean coupled energy budgets of tropical convective discharge–recharge cycles. *Journal of the Atmospheric Sciences*, 81(1), 3–29. https://doi.org/10.1175/JAS-D-23-0061.1
- Zhang, C., & Hagos, S. M. (2009). Bi-modal structure and variability of large-scale diabatic heating in the tropics. *Journal of the Atmospheric Sciences*, 66(12), 3621–3640. https://doi.org/10.1175/2009JAS3089.1

LI ET AL. 13 of 13